Journal of the Optical Society of America A
OPTICS, IMAGE SCIENCE, AND VISION

# Physiological wound assessment from coregistered and segmented tissue hemoglobin maps

E. A. Robledo,[1] R. Schutzman,[1] R. Fang,[2] C. Fernandez,[1] R. Kwasinski,[1] K. Leiva,[1] F. Perez-Clavijo,[3] and A. Godavarty[1,*]

[1]Optical Imaging Laboratory at Florida International University, Miami, Florida 33174, USA
[2]Biomedical Engineering Department, University of Florida, Gainesville, Florida 32611, USA
[3]Podiatry Care Partners Inc., Doral, Florida 33126, USA
*Corresponding author: godavart@fiu.edu

Received 15 April 2020; revised 1 July 2020; accepted 2 July 2020; posted 2 July 2020 (Doc. ID 394985); published 20 July 2020

**A handheld near-infrared optical scanner (NIROS) was recently developed to map for effective changes in oxy- and deoxyhemoglobin concentration in diabetic foot ulcers (DFUs) across weeks of treatment. Herein, a coregistration and image segmentation approach was implemented to overlay hemoglobin maps onto the white light images of ulcers. Validation studies demonstrated over 97% accuracy in coregistration. Coregistration was further applied to a healing DFU across weeks of healing. The potential to predict changes in wound healing was observed when comparing the coregistered and segmented hemoglobin concentration area maps to the visual area of the wound.** 

https://doi.org/10.1364/JOSAA.394985

## 1. INTRODUCTION

### A. Lower-Extremity Ulcers

Lower-extremity ulcers are one of the most common complications that has increased over the past few years [1]. The prevalence of lower-extremity ulceration is 0.18% to 2%, and in patients over 65 years of age, it is up to 5% [2]. In the United States, at least 4.6 million workdays are lost and over $1 billion is spent every year only for chronic venous ulcers [3]. During the long-term wound-healing process, an objective and quantitative determination of the wound-healing rate plays a crucial role in assessing the efficacy of treatments.

To date, lower-extremity ulcers are visually inspected by clinicians as a gold-standard approach, in order to determine if the ulcers are healing or not. The parameters used to assess wound healing include wound size reduction, change in wound color, and epithelization. Wound size is determined by measuring the largest width and length of the wound and determining the rectangular area. Many times the wounds are not rectangular, and hence there is an error and subjectivity in determining wound size. According to the Wound Healing Society (WHS), a reduction in wound size by ∼50% in 4 weeks relates to a healing wound. Hence, accurate quantified measurements of wound area are important for objective assessment. There are various image segmentation approaches that are appropriate for medical applications [4–9], many of which have been developed and applied for digitizing accurate wound size measurements [10,11]. Digitized wound size measurements remove subjectivity to a large extent, but they do not provide any physiological information to subclinically assess the progress of healing.

### B. Imaging Technologies to Assess Wound Healing

The gold-standard clinical approach of visually assessing the wound and its size is complemented by physiological assessment for tissue oxygenation changes. It has been demonstrated that oxygen is vital for wound healing [12]. Imaging techniques such as hyperspectral imaging (HSI) [4,5,11], multispectral imaging (MSI) [4], and near-infrared spectroscopy (NIRS) [4,13] have been developed by various research groups to obtain tissue oxygenation changes in the wound compared to its immediate surroundings. The wound-imaging technologies that employ near-infrared (NIR) light are capable of subsurface imaging. Researchers have employed Monte Carlo simulations of light propagation to simulate the detection limits (up to 3 mm) of these NIR-based technologies [14,15].

From past wound imaging studies, it was observed that increased oxygenation at the wound site (compared to the background) and its reduction with time (as the wound moves away from the inflammatory phase of healing) correlate to a healing wound [4]. These tissue oxygenation maps are visually correlated to the white light (i.e., visual) images of the wound. In some cases, researchers apply image segmentation techniques to the color and/or RGB images of wounds obtained from HSI [5]

in order to obtain digitized wound size measurements. However, to date, the tissue oxygenation maps have not been registered onto the white light images nor segmented to quantify the area of increased or decreased oxygenation.

### C. Medical Segmentation Techniques on Wound Images

Various segmentation techniques such as graph cut, active contour or grow cut, and regions growth have been applied for medical images. While active contour models (ACMs) are sensitive to the location of the initial contours [16,17], the region growth technique [4] relies on the seed points and maximum intensity distance to allow precise segmentation. Graph cut is a combinatorial optimization technique [18], where optimal pixel labeling can be efficiently computed by max-flow/min-cut algorithms automatically. In the area of wound imaging, most image segmentation approaches were related to applying a threshold or one of the above segmentation techniques on the RGB images of the wounds obtained from white light [4,6–10,19] or HSI images [4,5,11]. There have been no studies to date where segmentation of oxygenation maps was carried out to quantify the regions of increased or decreased oxygenation or hemoglobin concentrations.

Recently, a noncontact NIRS-based imaging device was developed to obtain hemoglobin concentration maps (including tissue oxygenation maps) of lower-extremity ulcers and assess potential to heal based on oxygenation based on wound:background (W:B) contrasts [13]. Herein, a graph-cut-based image segmentation approach has been implemented to segment the regions of increased (or decreased) hemoglobin concentration maps of diabetic foot ulcers, via longitudinal NIR imaging studies across weeks of treatment. Additionally, a combined coregistration and image segmentation approach was developed to coregister these hemoglobin concentration maps onto the color images of the wounds, along with demarcating and quantifying the area of increased (or decreased) hemoglobin concentration.

## 2. MATERIALS AND METHODS

### A. NIRS-Based Imaging

A handheld near-infrared optical scanner (NIROS) was employed for noncontact, portable imaging of lower-extremity ulcers (here, diabetic foot ulcers). This handheld device performs multiwavelength (725 nm and 797 nm) continuous-wave-based imaging to obtain diffuse reflectance signals of the wound and its surrounding regions [13]. The chosen wavelengths and system were tested for their probing depth by employing Monte Carlo simulations on five-layer skin tissue phantoms, which demonstrated probing depths up to 3 mm. The source distribution is calibrated using a uniform diffused white calibration sheet and in turn applied during the evaluation of the hemoglobin concentration maps from the dual-wavelength diffuse reflectance images (described further in Section 2.B.1) [13]. The calibration also accounts for the varying distance between the device and the wound during consecutive imaging studies of the wound across weekly treatment. A separate endoscopic/digital camera is employed alongside NIROS to acquire digital white light (or color) images apart from NIR images. Extensive details on the NIROS instrumentation are described in detail elsewhere [13].

#### 1. *In Vivo Imaging Study*

A Florida International University International Review Board (FIU-IRB) approved study (IRB approval #13-0092) was carried out at Podiatry Care Partners (Miami, FL) for imaging lower-extremity ulcers (here, diabetic foot ulcers, DFUs). A written consent and HIPAA authorization was obtained from all subjects. Although many subjects were recruited for our NIR imaging study, a single DFU case imaged across weeks of treatment (i.e., imaged intermittently across 23 weeks from the first imaging visit) was used in the current studies. In this DFU case, appropriate fiducial markers were placed around the DFU during imaging in order to facilitate coregistration apart from NIR imaging. The region of interest (DFU) was imaged thrice from different angles of the wound during each visit. One of these three images with the least skewness in the fiducial marker was selected for coregistration. This sample *in vivo* imaging case was used to demonstrate the implementation of the coregistration and segmentation approach onto hemoglobin concentration maps of the DFUs.

### B. Image Analysis Approach

Image analysis of the dual-wavelength diffuse reflected (NIR) images and white light (or color) images of the wound followed a series of steps as illustrated in Fig. 1. Initially the diffuse reflected images [Figs. 1(a) and 1(b)] acquired at two wavelengths

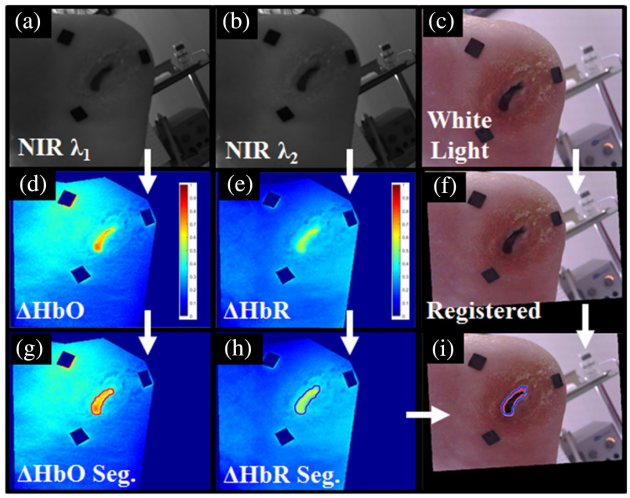


**Fig. 1.** Flowchart of the image processing approach. (a),(b) Diffuse reflectance acquired from NIROS. (c) White light image acquired from endoscopic camera. (d),(e) Effective hemoglobin concentration maps as obtained from NIR images. (f) Registered white light image with respect to the hemoglobin concentration maps. (g),(h) The demarcated region of changed hemoglobin concentration around the wound region. (i) The coregistered image of the demarcated boundaries of the segmented hemoglobin concentration maps onto the registered white light image. The red and the blue outlines represent the segmented boundaries of ΔHbO and ΔHbR, respectively. A DFU case (during week 16 of their visit) was used as a sample for this flowchart.

were employed to generate effective hemoglobin concentration maps in terms of oxy- (ΔHbO) and deoxy- (ΔHbR) hemoglobin [Figs. 1(d) and 1(e)] and total hemoglobin (ΔHbT = ΔHbO + ΔHbR). The obtained concentration maps were further segmented to isolate regions of increased/decreased hemoglobin concentrations [Figs. 1(g) and 1(h)]. In parallel, the digital white light image [Fig. 1(c)] was spatially aligned with respect to the diffuse reflected NIR images of the wound [Fig. 1(f)] to obtain a registered image. As a final step, the demarcated boundaries (or traces) of the segmented hemoglobin regions are overlaid (i.e., coregistered) onto the registered white light images [Fig. 1(i)]. This was carried out to quantify the areas of increased/decreased hemoglobin concentrations in comparison to the visual (white light) wound size that was measured by the clinician.

### 1. Hemoglobin Concentration Maps

The modified Beer–Lambert's law (MBLL) was employed to determine effective changes in oxy- (ΔHbO) and deoxy- (ΔHbR) hemoglobin concentrations using the diffuse reflectance images obtained at both the wavelengths. A calibration image (using a uniformly diffused white sheet) at each wavelength was used as a reference image during hemoglobin concentration analysis [13]. Dark current noise was also accounted for during imaging studies. Further details of the hemoglobin concentration map analysis are provided elsewhere [13]. The effective hemoglobin concentrations (ΔHbO, ΔHbR, and ΔHbT) were estimated during each imaging visit by the subject and compared across weeks of treatment. An example of a 2D hemoglobin concentration map of the DFU case (week 16) is given in Figs. 1(d) and 1(e).

### 2. Registration Approach

The registration technique was applied using a transformation matrix approach employing specific markers across both the white light image and the hemoglobin concentration maps. Fiducial markers were placed around the wound region to assist in the registration process and also to quantify area of the segmented regions. Since both the white light image and the NIR image contain the same shapes (i.e., fiducial markers), the transformation matrix can be created using "nonreflective similarity." The transformation matrix was further employed to align the moving white light image with respect to the 2D spatial references of the hemoglobin concentration maps. Figure 1(c) demonstrates an example of the white light image of a DFU case (week 16 of the imaging study) [Fig. 1(f)], whose size and orientation were aligned to that of the corresponding hemoglobin map(s) [Figs. 1(a) and 1(b)]. The white light image that was registered with respect to the hemoglobin concentration map tends to lose some of its pixel data from the transformation and change in pixel resolution.

### 3. Validation of the Registration Technique

Phantom and *in vivo* studies were performed to validate the accuracy of the developed coregistration technique. Three ideal scenarios were designed to test the accuracy of the technique. In study 1, a flat surface phantom was imaged using a flat white sheet of thin paper. In study 2, a curved surface solid phantom (mimicking the surface of the skin) was imaged using a white cylindrical surface of diameter 10 cm. In study 3, registration study was performed *in vivo* on the right leg (IRB approved) under normal conditions.

In all three studies, fiducial markers of various shapes and sizes were placed onto the respective surface and imaged to obtain the diffuse reflected NIR image (at a single wavelength) and white light image. The white light image was spatially aligned (or registered) with respect to the NIR image. Each imaging study was repeated thrice. The markers were segmented using the kernel graph-cut technique (described further in Section 2.B.3) in both the registered white light image (also termed as color or RGB) and NIR image(s).

Accuracy of the registration (or spatial alignment and overlay of images) was calculated from the percentage overlap of the segmented regions across the NIR and white light images by employing a subtraction technique. The segmented fiducial markers obtained from the registered white light image were subtracted from the segmented markers from the NIR image:

$$\mathbf{A}_{i,j} = \begin{cases} 1 & (x_i, y_j) \in \mathbf{R} \\ 0 & (x_i, y_j) \notin \mathbf{R} \end{cases}, \tag{1}$$

$$\mathbf{B}_{i,j} = \begin{cases} 1 & (x_i, y_j) \in \mathbf{R} \\ 0 & (x_i, y_j) \notin \mathbf{R} \end{cases}. \tag{2}$$

$\mathbf{A}_{i,j}$ and $\mathbf{B}_{i,j}$ denoted the logical matrix created for the NIR image and registered white light image, respectively. $\mathbf{R}$ is the domain of pixels that were segmented. $x_i$ and $y_j$ denote the pixel value and location within the NIR and registered image. The segmented markers of the registered white light image were subtracted from the segmented markers of the NIR image (i.e. $\mathbf{A}_{i,j} - \mathbf{B}_{i,j}$).

The pixel indices with matching pixels (MP) will result in a value of zero:

$$\mathbf{MP}_{i,j} = (\mathbf{A}_{i,j} - \mathbf{B}_{i,j} == 0). \tag{3}$$

All indices with a 1 value imply that the pixel values were matching across both images at the specific location $(i, j)$. The overlap percentage depended on how much of the segmented region spatially aligned across the NIR image (at a single wavelength) and the registered white light image, which thus determined the accuracy of registration:

$$\text{Accuracy}_{\text{registration}} = \frac{\sum_{i,j=1}^{n,m} \mathbf{MP}_{i,j} \times 100}{n \times m}. \tag{4}$$

### 4. Segmentation Approach

Various segmentation techniques such as graph-cut, active contour, or growcut region growth have been applied for medical images [4–9]. In this study, the kernel-based graph-cut algorithm that was developed by prior researchers for other applications [20,21] was employed to segment hemoglobin concentration maps. Graph cut is a useful tool for accurately segmenting any type of image that guarantees a global solution since it is independent of a chosen initial center point. This

semi-automated algorithm exploits similar gray values of pixels that are close neighbors and groups them into nodes. A weight is provided between different regions of similar pixel values or nodes. The segmentation partitions the image using combinatorial optimization to ensure a globally minimum cut of the image. A cut is defined by the sum of the weights of the edges that it severs [20]. A schematic of the kernel graph-cut technique example on a 3 × 3 pixel region is shown in Fig. 2. The pixels are grouped into two special nodes called terminals (background and object terminal). Similarity between terminals defines the weight of their edges. In Fig. 2, the thickness of the lines increases with an increase in the difference between the nodes. A minimum cost cut is generated based on the weight of the edges between the terminals' resistance. Upon employing a multiregion graph-cut segmentation technique and applying the kernel-mapping formulation, several regions will be segmented depending on their pixel values [21].

The graph-cut algorithm suits the needs of wound segmentation because it can be easily manipulated to see small degrees of changes in hemoglobin concentrations. The segmentation process can isolate several regions or layers of increased (or decreased) hemoglobin concentration within or around the wound. Furthermore, quantifying the area of these segmented regions (representing regions of increased or decreased hemoglobin concentrations) can assist in correlating the area of physiological changes to visual wound size reduction during healing. Other rudimentary segmentation techniques employ pixel grayscale thresholds at different percentages (20%, 40%, etc.) in order to segment a wound. The threshold-based technique can be flawed due to subjectivity in choosing the threshold value, which can possibly remove necessary information or alternatively retain noise.

The graph-cut technique requires two input parameters: the 2D hemoglobin concentration data and a kernel value. The

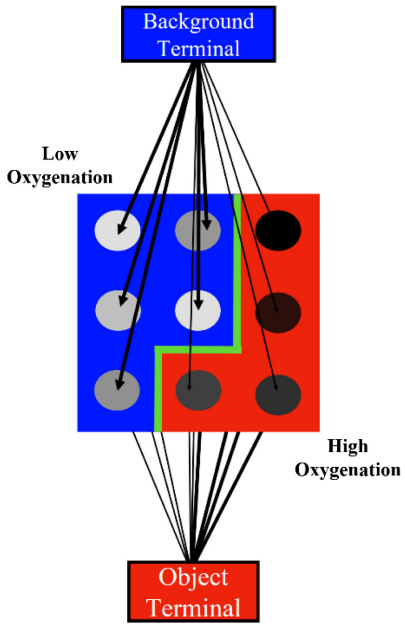


**Fig. 2.** Schematic of the kernel graph-cut algorithm on a 3 × 3 pixel region. Pixels are grouped into special nodes called terminals. The bold black arrows link the pixels to their corresponding terminals.

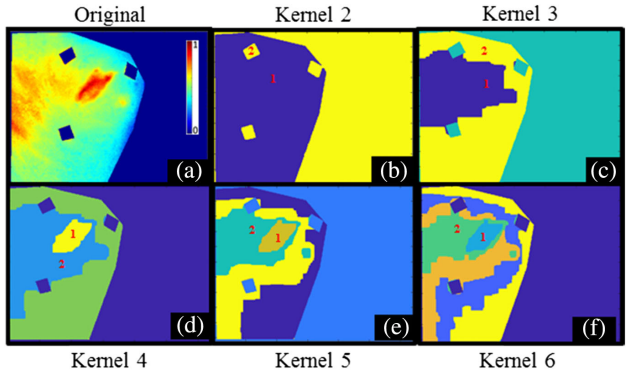


**Fig. 3.** Kernel graph cut of ΔHbO for a DFU case (from week 4 of the imaging study). (a) The ΔHbO map prior to segmentation; (b)–(f) segmented regions for various input kernel numbers. The segmented region close to the wound region is labeled "1," and the adjacent segmented region is labeled "2." This labeling is used in kernel selection.

kernel value will affect the number of regions of the hemoglobin concentration image (a pseudo-color plot of the 2D data) that will be segmented into depending on the weight between the pixel value groups. Figure 3 is an example case of a DFU (week 4 of the imaging study), wherein the effect of various kernel values on the segmented areas in both the hemoglobin concentration maps (ΔHbO and ΔHbR) are given. Regions of increased ΔHbO and decreased ΔHbR are segmented in the current example case. With a smaller kernel number, the background noise (i.e., region outside the imaged foot) and the fiducial markers were segmented. The later kernels segmented the regions of changed hemoglobin concentration as seen in Figs. 3(d)–3(f). The region that most encompasses the wound (observed from white light images) is chosen and isolated for analysis. The choice of the kernel number may vary for each image, requiring operator dependency in its choice during segmentation. Hence, a method to automate the kernel selection was developed.

### 5. Kernel Selection

Kernel selection can be manual or automated. The subjectivity in segmentation can be avoided by automating the kernel selection process. A method was developed to determine the optimal kernel number to segment a given wound image. The effective hemoglobin concentration difference between the first and second segmented regions (as shown in Fig. 3, numbered as 1 and 2) for the different cases of kernel number selection were determined and plotted against the kernel number. More specifically, a 5 × 5 pixel area was extracted from these two adjacent segmented regions (1 and 2), and their averaged effective hemoglobin concentration subtracted from each other. The differences were calculated at three random locations within these two segmented regions (1 and 2), and the average effective hemoglobin concentration differences (or simply, average hemoglobin contrast) were compared to that acquired from similar analysis using different kernel values during segmentation of the same data set. Figure 4 shows (sample case of DFU from week 16) that as the kernel number increases, the average

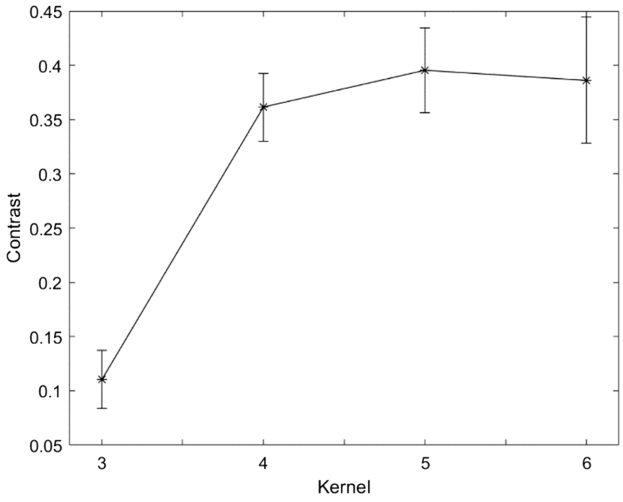


**Fig. 4.** Plot of average hemoglobin contrast (or differences between segmented regions 1 and 2) and the respective error bar versus kernel values obtained from the ΔHbO map of the DFU case (week 16 of the imaging study). The error bar represents the standard deviation across the three random contrast values obtained from three random trials within segmented regions 1 and 2.

hemoglobin contrast levels off from kernel 5 onwards. The error bar in Fig. 4 was obtained from the three random locations selected for averaging the effective hemoglobin contrast within the regions for each kernel. A similar trend was observed when segmenting both the ΔHbO and ΔHbR maps of the DFU case (across all weeks), where the average hemoglobin contrast did not change after a certain kernel number. This kernel number where average hemoglobin contrast variations diminished was different for each map and data set.

A sample pseudo-color image of the segmented ΔHbO (DFU case, week 4 of the imaging study) depicting only the first segmented boundary (that is, within the visual wound region) when employing kernel numbers 3, 4, 5, and 6 is shown in Fig. 5. In this case, beyond kernel number 6, the segmented area

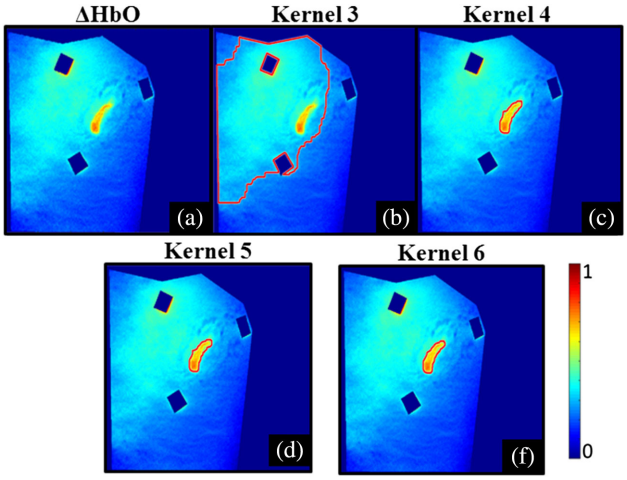


**Fig. 5.** ΔHbO maps of the DFU case (week 16 of the imaging study), with (a) no segmentation applied; (b), (c), (d), and (f) kernel values 3, 4, 5, and 6, respectively, utilized to segment the maps. The red demarcated boundary is that of the first segmented region (encompassing the visual wound) for each kernel value chosen.

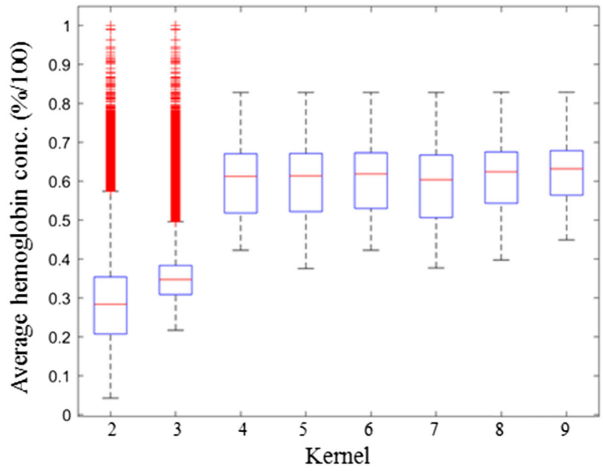


**Fig. 6.** Boxplot of average hemoglobin concentration from the first segmented region when choosing different kernel values during kernel graph-cut segmentation. Here the hemoglobin concentration is that of ΔHbO from week 16's data of the DFU.

of the first region did not change. In other words, the average hemoglobin contrast variations diminished beyond kernel number 6. The approach described via these pseudo-color plots (Fig. 5) and average hemoglobin contrast plots (Fig. 4) can be used to automate the kernel selection process during segmentation. This approach was also quantified to further validate the kernel selection process via a statistical approach.

The statistically relevant quantitative approach for operator-independent kernel selection is using the average and standard deviation across a single segmented region in the hemoglobin concentration map. A boxplot of the average and standard deviation of the hemoglobin concentration from the first segmented region was plotted for each kernel value in Fig. 6 (sample DFU case from week 16 of the imaging study). As the kernel value increases, the average concentration across the kernels varies minimally. The optimal kernel value for each data was chosen when this average concentration varied $\leq 5\%$, when comparing the first segmented region across each chosen kernel value. In the sample case shown in Fig. 5, qualitatively the optimal kernel value was 4, which was further confirmed from the statistical analysis in Fig. 6. By employing an objective approach to kernel selection (contrast and statistical analysis), operator dependency can be removed. This automated kernel selection process, along with other attributes, can be implemented in machine learning algorithms (in the future) to further automate the entire segmentation and coregistration approach.

The demarcated boundaries of the first segmented region (using the optimal kernel value) ΔHbO, ΔHbR, and ΔHbT were coregistered onto the spatially aligned white light image of the wound. These demarcated boundaries (or traces) of hemoglobin concentrations were in turn quantified via area calculations and compared to the area of the wound (from white light images).

### 6. Area Calculation

The fiducial markers placed around the DFU were employed for estimating the area of the segmented regions of the hemoglobin

concentration maps, apart from assisting in the coregistration process. Fiducial markers were segmented only from the white light images for area calculation instead of the hemoglobin concentration maps or NIR images because the white light images reflect the true area of the fiducial markers. The area of a contour can be calculated using the pixel ratio between the segmented marker(s), the segmented hemoglobin concentration map, and the known marker size ($0.635 \times 0.635$ cm$^2$). Area calculations were employed to compare the visual wound size and the area of changed hemoglobin concentration across weeks of treatment. The visual wound size was physically measured by the clinician (during weekly treatment) in terms of its length and width, in order to calculate the white light wound area.

Imaging of wounds typically occurs on a curved surface, especially when focusing on lower-extremity wounds. This makes the placement of the fiducial marker and the angle of imaging crucial in registration as well as area calculations. Thus, the fiducial marker, which is on the same 2D plane as the wound, is chosen for registration as well as area calculations to avoid errors from curvatures.

## 3. RESULTS

### A. Registration Validation Study

The NIR images of the fiducial markers were segmented, and the segmented boundaries were coregistered onto the registered white light images of the markers in all three phantom studies. Sample data for each study (flat phantom, curved phantom, and *in vivo* curved surface) of the coregistered images are shown in Fig. 7. Qualitatively, it can be seen that the segmented boundaries (or traces) of the NIR images (in red) coregister accurately with the registered white light images. The quantitative accuracies from each case and across three repeated studies are given in Table 1, demonstrating an average accuracy of 98.7% across all cases. The accuracy of registering the images was less in the curved phantom when compared to an *in vivo* case (97.6% versus 99.1%). This is possibly due to greater curvature of the phantom than the subject's leg, causing difficulties in matching the spatial orientation between the white light and NIR images. Having validated the registration accuracy, the process of registration and coregistration of the hemoglobin concentration traces are described in the following sections.

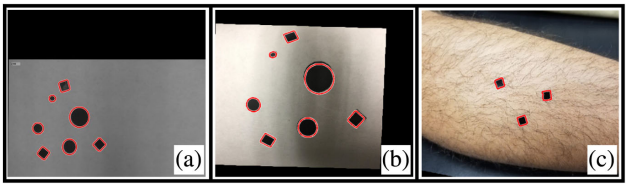


**Fig. 7.** Coregistration of the demarcated boundaries of the segmented NIR images (red color) onto the registered white light images, for (a) a flat surface phantom, (b) a curved-surface phantom, and (c) an *in vivo* curved leg surface.

**Table 1. Accuracy and Standard Deviation of the Registration Between NIR and White Light Images as Obtained from Phantom and *In Vivo* Imaging Study**

| Study | Accuracy |
|---|---|
| Flat-surface phantom | 99.3%±0.34% |
| Curved-surface phantom | 97.6%±1.10% |
| *In Vivo* curved leg surface | 99.1%±0.88% |

### B. Segmentation of Hemoglobin Maps in DFUs

A DFU case with a healing wound was imaged at discrete weeks (based on patient availability) across a 17-week longitudinal study during its treatment. Imaging studies performed during weeks 1–3 were not included because, during these initial studies, white light images of the DFU were not acquired towards coregistration analysis. The clinician noted several changes in the skin condition surrounding the wound throughout the study as shown in the white light images in Fig. 8. During weeks 4 and 5, the subject had periwound erythema and localized cellulitis that improved over weeks with treatment. During the following weeks, the skin developed dermatitis and xerosis. Overall, this was a healing DFU as observed (by the clinician) from the first week of imaging, but at a slower pace. The ΔHbO and ΔHbR maps obtained during weeks 4, 5, 15, 16, and 17 of the imaging study are shown in Fig. 8. The hemoglobin concentration traces (i.e., demarcated boundaries after segmentation) were coregistered onto the registered white light images as shown in Fig. 8 (as the last column) [22] (part of these results published in SPIE conference proceedings). The area within ΔHbO, ΔHbR, and ΔHbT trace is calculated (as described

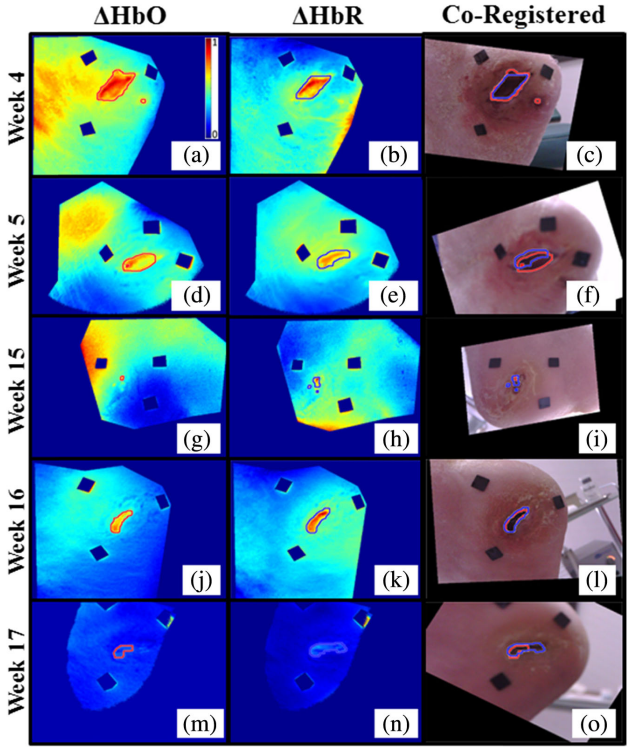


**Fig. 8.** 2D pseudo-color maps of ΔHbO and ΔHbR across weeks of imaging a healing DFU case. The last column [(c), (f), (i), (l), (o)] shows the coregistered images of ΔHbO and ΔHbR segmented traces overlaid on the registered white light images for the respective weeks. The three black (or dark) squares are the fiducial markers. The demarcated boundaries (or traces) for ΔHbO and ΔHbR are shown in red and blue, respectively.

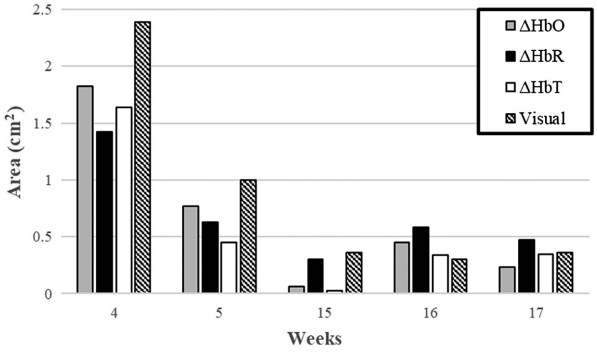


**Fig. 9.** Bar plot displaying the area of the segmented regions of ΔHbO, ΔHbR, and ΔHbT, along with the visual wound area (determined by the clinician) across different weeks of imaging a healing DFU.

in Section 2.B.4) and compared to the visual wound area (as determined by the clinician) in Fig. 9.

## 4. DISCUSSION

Coregistered images containing physiological information along with the visual wound details is essential for clinicians to directly correlate physiology to anatomical changes in the DFUs during treatment. Having validated the accuracy of the coregistration process (over 97%) from phantom and *in vivo* studies, the developed segmentation and coregistration technique can be applied to wound or any tissue imaging application. In the current study, where a healing DFU case was imaged across multiple weeks during its treatment, the longitudinal analysis of the physiological status of the wound along with the visual status proved useful. From the ΔHbO and ΔHbR maps across weeks, it was observed that the hemoglobin concentrations are elevated around the wound site. As the wound healed, the area of increased hemoglobin concentration reduces. Past work has demonstrated that when wounds are in the inflammatory phase, their hemoglobin concentrations are higher at the wound site in comparison to the surroundings [23]. Upon healing, the wound moves away from the inflammatory phase, and hence its hemoglobin concentrations decrease and become closer to that of the wound as it heals. The area of increased hemoglobin concentrations reduces with healing as observed from Fig. 9.

From Figs. 8 and 9, it can also be seen that visual wound area (or size) was decreasing, depicting healing. A 58.2% reduction in visual wound size was observed from week 4 to week 5 and ∼85% by week 15. The wound began to open slightly as clearly observed qualitatively from Fig. 8, but not from quantitative measurement (as shown in Fig. 9). The ineffective quantitative assessment is because all clinical measurements of the wound area are based on length × width (applicable only for rectangular or square wounds), while the current DFU is irregular in shape. The area of increased ΔHbO was relatively higher than the area of ΔHbR in weeks 4 and 5. From week 15 onwards, the area of ΔHbR was relatively higher than the area of ΔHbO. During week 16, the wound opened up, and the area of increased ΔHbR was elevated in comparison to the area of increased ΔHbO. This possibly implies that an increase in the area of ΔHbR over ΔHbO may indicate a possible reversal to healing or the wound opening up. Physiologically this may have been indicative (in week 15) prior to the anatomical increase in wound size (in week 16). The changes in the area of increased ΔHbT follows a similar trend to that of ΔHbO. This is a preliminary observation that required application of the coregistration and physiological area measurement approach. The proposed approach will be applied on a large sample size of DFUs as part of our future work.

Ongoing efforts are to fully automate the coregistration process at various stages, including kernel value selection, segmentation approaches to demarcate the visual area of the wound (instead of manual length × width measurements), and automated registration of the white light images with respect to hemoglobin concentration maps. This automation will also involve machine learning tools to effectively remove operator dependency.

## 5. CONCLUSIONS

A NIROS was used to image for effective changes in ΔHbO and ΔHbR in DFUs, across weeks of treatment. An image processing approach was implemented to segment regions of increased (or decreased) hemoglobin concentrations around the visual wound region and coregister the traces (or boundaries) onto the registered white light images of the wound. The developed approach to segment hemoglobin concentration maps and coregister them onto their digital white light counterpart has potential to further advance the wound assessment process. Using this physiological counterpart to the visual wound details allows for objective and subclinical wound assessment during weekly treatment (and, in the future, possibly lead to effective and earlier interventions in wound care management).

**Funding.** Florida International University FIU-BME (Biomedical Engineering) & FIU-CEC (College of Engineering) Coulter Seed Funds and Coulter Undergraduate Research Excellence (CURE) Program.

**Acknowledgment.** We thank the staff at Podiatry Care Partners for the assistance during clinical imaging studies.

**Disclosures.** The authors declare no conflicts of interest.

## REFERENCES

1. S. V. Agale, "Chronic leg ulcers: epidemiology, aetiopathogenisis, and management," Ulcers **2013**, 1–7 (2013).
2. S. D. Ramsey, K. Newton, D. Blough, D. K. McCulloch, N. Sandhu, G. E. Reiber, and E. H. Wagner, "Incidence, outcomes, and cost of foot ulcers in patients with diabetes," Diabetes Care **22**, 382–387 (1999).
3. G. Spentzouris and N. Labropoulos, "The evaluation of lower-extremity ulcers," Semin. Intervent. Radiol. **26**, 286–295 (2009).
4. R. Mukherjee, S. Tewary, and A. Routray, "Diagnostic and prognostic utility of non-invasive multimodal imaging in chronic wound monitoring: a systematic review," J. Med. Syst. **41**, 46 (2017).
5. L. A. Paluchowski, H. B. Nordgaard, A. Bjorgan, H. Hov, S. M. Berget, and L. L. Randeberg, "Can spectral-spatial image segmentation be used to discriminate experimental burn wounds?" J. Biomed. Opt. **21**, 101413 (2016).

6. H. Lu, B. Li, J. Zhu, Y. Li, Y. Li, X. Xu, L. He, X. Li, J. Li, and S. Serikawa, "Wound intensity correction and segmentation with convolutional neural networks," Concurrency Comput. **29**, e3927 (2016).
7. H. Oduncu, A. Hoppe, M. Clark, and K. G. Harding, "Analysis of skin wound images using digital color image processing: a preliminary communication," Int. J. Low. Extrem. Wounds **3**, 151–156 (2004).
8. B. Jalil, O. Salvetti, L. Poti, M. Marinelli, V. Hartwig, A. L'Abbate, and S. Burchielli, "Segmentation using near-infrared imaging: an application to skin de-oxygenation," in *European Modelling Symposium* (IEEE, 2013), pp. 144–147.
9. V. Bochco, P. Välisuo, T. Harju, and J. Alander, "Lower extremity ulcer image segmentation of visual and near-infrared imagery," Skin Res. Tehchnol. **16**, 190–197 (2010).
10. A. Körber, J. Rietkötter, S. Grabbe, and J. Dissemond, "Three-dimensional documentation of wound healing: first results of a new objective method for measurement," J. Dtsch. Dermatol. Ges. **4**, 848–854 (2006).
11. J. Marotz, A. Siafliakis, A. Holmer, A. Kulcke, and F. Siemers, "First results of a new hyperspectral camera system for chemical based wound analysis," Wound Med. **10-11**, 17–22 (2015).
12. S. Schreml, R. M. Szeimies, L. Prantl, S. Karrer, M. Landthaler, and P. Babilas, "Oxygen in acute and chronic wound healing," Br. J. Dermatol. **163**, 257–268 (2010).
13. K. Leiva, J. Mahadevan, K. Kaile, R. Schutzman, E. Robledo, S. Narayanan, V. Muthukrishnan, V. Mohan, W. Wu, and A. Godavarty, "Breath-hold paradigm to assess variations in oxygen flow in diabetic foot ulcers using a noncontact near-infrared optical scanner," Adv. Wound Care **8**, 386–402 (2019).
14. T. Binzoni, A. Vogel, A. H. Gandjbakhche, and R. Marchesini, "Detection limits of multi-spectral optical imaging under the skin," Phys. Med. Biol. **53**, 617–636 (2008).
15. J. E. Thatcher, J. J. Squiers, S. C. Kanick, D. R. King, Y. Lu, Y. Wang, R. Mohan, E. W. Sellke, and J. M. DiMaio, "Imaging techniques for clinical burn assessment with a focus on multispectral imaging," Adv. Wound Care **5**, 360–378 (2016).
16. K. Zhang, L. Zhang, K. M. Lam, and D. Zhang, "A locally statistical active contour model for image segmentation with intensity inhomogeneity," arXiv:1305.7053 (2013).
17. L. Liu, Q. Zhang, M. Wu, W. Li, and F. Shang, "Adaptive segmentation of magnetic resonance images with intensity inhomogeneity using level set method," Magn. Res. Imaging **31**, 567–574 (2013).
18. P. F. Felzenszwalb and D. P. Huttenlocher, "Efficient graph-based image segmentation," Int. J. Comp. Vis. **59**, 167–181 (2004).
19. R. Mukherjee, D. D. Manohar, D. K. Das, A. Achar, A. Mitra, and C. Chakraborty, "Automated tissue classification framework for reproducible chronic wound assessment," Biomed. Res. Int. **2014**, 851582 (2014).
20. Y. Y. Boykov and M. P. Jolly, "Interactive graph cuts for optimal boundary & region segmentation of objects in N-D images," in *8th IEEE International Conference on Computer Vision* (IEEE, 2001), pp. 105–112.
21. M. B. Salah, A. Mitiche, and I. B. Ayed, "Multiregion image segmentation by parametric kernel graph cuts," IEEE Trans. Image Process. **20**, 545–557 (2011).
22. E. Robledo, R. Schutzman, R. Fang, C. Fernandez, R. Kwasinski, K. Leiva, F. Perez-Clavijo, and A. Godavarty, "Semi-automated machine learning approach to segment and register tissue oxygenation maps onto clinical images of wounds," Proc. SPIE **10873**, 1087305 (2019).
23. E. S. Papazoglou, M. Neidrauer, L. Zubkov, M. S. Weingarten, and K. Pourrezaei, "Noninvasive assessment of diabetic foot ulcers with diffuse photon density wave methodology: pilot human study," J. Biomed. Opt. **14**, 064032 (2009).